Estimation of the Laser Frequency Noise Spectrum by Continuous Dynamical Decoupling

Manchao Zhang,[1,2] Yi Xie,[1,2] Jie Zhang,[1,2] Weichen Wang,[1,2] Chunwang Wu,[1,2] Ting Chen,[1,2] Wei Wu,[1,2,*] and Pingxing Chen[1,2,†]

[1] *Department of Physics, College of Liberal Arts and Sciences, National University of Defense Technology, Changsha Hunan 410073, China*

[2] *Interdisciplinary Center for Quantum Information, National University of Defense Technology, Changsha, Hunan 410073, China*

(Received 2 July 2020; revised 21 October 2020; accepted 23 December 2020; published 20 January 2021)

Decoherence induced by laser frequency noise is one of the most important obstacles in quantum information processing. In order to suppress this decoherence, the noise power spectral density needs to be accurately characterized. In particular, the noise spectrum measurement based on the coherence characteristics of qubits would be a meaningful and still challenging method. Here, we theoretically analyze and experimentally obtain the spectrum of laser frequency noise based on the continuous dynamical decoupling technique. We first estimate the mixture-noise (including laser and magnetic noises) spectrum up to $(2\pi)530$ kHz by monitoring the transverse relaxation from an initial state $+X$, followed by a gradient descent data process protocol. Then the contribution from the laser noise is extracted by encoding the qubits on different Zeeman sublevels. We also investigate two sufficiently strong noise components by making an analogy between these noises and driving lasers whose linewidth is assumed to be negligible. This method is verified experimentally and finally helps to characterize the noise.

DOI: 10.1103/PhysRevApplied.15.014033

I. INTRODUCTION

The problem of a quantum system interacting with a noisy environment is of great significance in the field of quantum computing [1]. In general, there are some strategies to fight this decoherence and improve the fidelity of quantum operations. One method is based on error-correction protocols by encoding multiple physical qubits into a logical qubit, which of course requires a tremendous amount of qubit resources [2]. The second method is reducing the amplitude of environmental noise. This can be realized by applying a reverse compensation signal targeting the interested noise [3]. Or in contrast, reduce the system's internal sensitivity to noise through the application of coherent control-pulse methods [4–9] or encoding the information to pairs of dressed states that are formed by concatenated continuous driving fields [10–16]. However, the latter two approaches depend on the prior knowledge of the noise power spectral density (PSD) [17,18].

Laser frequency noise or phase noise describes how the frequency of a laser field deviates from an ideal value. This quantity, which is defined to evaluate the short-term stability of a laser, has attracted widespread attention as a fundamental topic about lasers. Generally, the noise features of a laser can be revealed through the following two schemes. One is the optical heterodyne method that contains two different categories. The first category is comparing the laser with itself through the delayed self-heterodyne scheme [19]. For an ultranarrow-linewidth laser, at least hundreds of kilometers of optical fiber are required to realize a delay time longer than the laser coherent time. The other category is comparing the frequency of a target laser with reference lasers by the light-beam heterodyne method, which is also called the beat-note method in some articles [20]. If the target laser is beat with only one reference laser, we get an electrical signal that contains noise information of both lasers, but fail to separate their contributions. Instead, if two reference lasers are introduced in the experiment, two electrical signals can be detected. These signals are first mixed down to a lower frequency and then analyzed by a digital cross-correlation method to characterize the frequency noise PSD of the target laser [21]. In other words, to obtain the noise PSD, we have to set up at least other two similar lasers. This is uneconomic and has limited applications. The other method is referring the laser frequency to the atomic energy levels. The Rabi spectrum protocol, for example, can be used for PSD characterization by using

*weiwu@nudt.edu.cn
†pxchen@nudt.edu.cn

a weak and long excitation pulse. But the result can only be used as a reference as the accuracy is insufficient.

Another simple and effective technique for noise PSD estimation is called pulsed dynamical decoupling (PDD) [22–26]. PDD consists of applying π pulses, X_π or Y_π, to the system with designed intervals, which counteracts the coherence decay due to the noise, such as the Carl-Purcell-Meiboom-Gill [27] and Uhrig dynamical decoupling [28] sequences. In general, beside the laser frequency noise, laser power fluctuations and magnetic field fluctuations are also very important noise sources in quantum information processing, especially for many solid-state qubits. If the laser power fluctuations are suppressed in the experimental setup, the other two single-axis noises will be dominant, and affect the qubit evolution in a similar way [29]. Based on different quantum systems, the PDD technique has been utilized to extract the contributions of single magnetic noise [9,30] or laser frequency noise [31]. However, for practical applications, there also exist some drawbacks of PDD. On the one hand, the finite π-pulse length cannot be ignored in the experiments, and this will complicate the derivation of the filter function, which is the key tool for extracting the noise spectrum [32]. On the other hand, a large number of imperfect, finite-width pulses provoke the accumulation of errors (such as the pulse width error) and degrade the PDD performance [33]. Although these errors can be compensated or eliminated by additional sequence design and operations, the complexity of PDD increases [31]. This makes the protocol inefficient when the fidelity of a single π-pulse operation is not qualified.

An alternative approach is the continuous dynamical decoupling (CDD) technique where a continuous driving field is used instead of π pulses in PDD [16,34]. Compared to PDD, the concise, unimodal filter function as well as simple, high fidelity operations ensure better performance of CDD. In this paper, we mainly apply the CDD approach to the spectral estimation of laser frequency noise in a trapped ion system. We also propose a "laser-like noise" method (see Sec. III) for the characterization of two strong components, as well as the frequency region around them, of laser noise in our system. Note that, compared to the conventional optical heterodyne approach, these methods are actually handy and economical for characterizing the interested manipulation lasers. And the laser noise spectrum obtained here can be used for: (i) prolonging the coherence time and improving manipulation fidelity by choosing appropriate experimental parameters; (ii) improving the laser performance by analyzing and then controlling the noise sources.

The remainder of this paper is organized as follows. In Sec. II we review the fundamental CDD protocol and provide the control sequences in the experiments. In Sec. III we propose and experimentally validate an alternate noise characterization scheme adapted to the strong noise situation. Then the main result of this paper is given in Sec. IV where the PSD of the laser frequency noise is obtained. In Sec. V we compare the noise spectra based on our scheme with beat-note results. Finally, we conclude in Sec. VI.

II. THEORETICAL MODEL AND CONTROL SETTING

For the present experiment, we use a single $^{40}Ca^+$ ion confined in a standard blade trap. A pair of Zeeman sublevels in the $^2S_{1/2}$ and $^2D_{5/2}$ manifolds are used as a qubit, as shown in Fig. 1(a). We note that the magnetic fluctuation-induced decoherence is distinguishable for different qubit definitions, so we employ transitions $|1\rangle = |^2S_{1/2}, m_j = -\frac{1}{2}\rangle \leftrightarrow |2\rangle = |^2D_{5/2}, m_j = -\frac{1}{2}\rangle$ and $|1\rangle \leftrightarrow |3\rangle = |^2D_{5/2}, m_j = -\frac{5}{2}\rangle$ as magnetic noise and thus laser noise probes, on which the same pulse sequences [as the inset in Fig. 1(b)] are performed. In the experiment, we initialize the qubit to state $|1\rangle$ by Doppler cooling, sideband cooling, as well as optical pumping methods. Then a $\pi/2$ σ_y ($Y_{\pi/2}$) pulse is applied to rotate the qubit by 90° to the $+\sigma_x$ axis. During the driving evolution process, the 729 nm laser beam along σ_x is turned on for time t, followed by another $\pi/2$ σ_y pulse. The final state is discriminated using a fluorescence detection scheme.

For the driving evolution steps, we consider a two-level system (TLS) subjected to noises from the manipulation laser and magnetic field fluctuations. For resonant driving along the σ_x axis with Rabi frequency Ω, the Hamiltonian describing the qubit system in the rotating frame can be

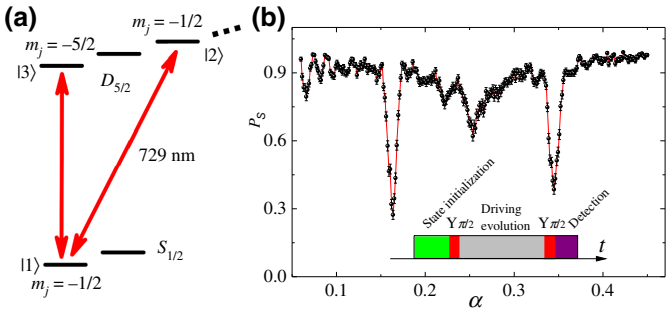

FIG. 1. Level structure and control sequence. (a) Scheme of two-level systems driven by a 729 nm laser. (b) Survival probability P_s as a function of the 729 nm laser strength α for $t = 200$ μs and transition $|1\rangle \leftrightarrow |3\rangle$. By checking α with Ω, we find that P_s has two local minimum values smaller than 0.5 at $\Omega \approx (2\pi)82$ and $(2\pi)164$ kHz. They can be viewed as two sufficiently strong noise components that do not follow the rules of Eq. (2) and should be modeled in another way. It should be mentioned that the linewidth around these components simply represents a power broadening as well as a Fourier limit instead of the linewidth of the electrical signal driving the etalon. Each point represents 200 experiments, and the error bars denote the projective measurement errors.

written as ($\hbar = 1$)

$$H = f(t)[\cos(\Omega t)\sigma_z + \sin(\Omega t)\sigma_y]/2. \quad (1)$$

Here, $f(t) = f_B(t) - f_L(t)$ (in radians) is the mixture noise in the time domain, and $f_B(t)[f_L(t)]$ represents the contribution from magnetic field (laser frequency) fluctuations. Generally, $f(t)$ can be treated as a stationary, Gaussian-distributed function with zero mean, i.e., $\langle f(t)\rangle = 0$. The statistics of this stochastic process $f(t)$ is fully determined by its autocorrelation function $C(t_1 - t_2) = \langle f(t_1)f(t_2)\rangle$, or equivalently by its power spectral density defined by the Fourier transform of $C(t)$: $S(\omega) = \int_{-\infty}^{\infty} C(t)e^{-i\omega t}dt$ (Wiener-Khinchin theorem).

In the weak noise limit, the connection between the driving evolution time t and the survival probability P_s of the qubit in state $+X$ can be derived based on the stochastic Liouville theory and superoperator formalism [35]. When we consider up to only the second-order cumulant,

$$P_s(t) = \frac{1}{2} + \frac{1}{2}\exp\left[-\int_0^{\infty} d\omega S(\omega)F(\omega,\Omega,t)\right], \quad (2)$$

where $F(\omega,\Omega,t) = t^2\{\mathrm{sinc}^2[(\omega+\Omega)t/2] + \mathrm{sinc}^2[(\omega-\Omega)t/2]\}/4\pi$ is the filter function characterized by t, Ω and peaked at $\omega = \pm\Omega$ with full width at half maximum $2\pi/t$ rad. This means that the performance of the sequence is sensitive to the characteristics of the noise, and we can get some sketchy but impressive information about the noise strength at Fourier frequency $\omega = \Omega$ by simply scanning Ω.

With $t = 200$ μs, we obtain the survival probability P_s as a function of α, which refers to the 729 nm laser amplitude modulation used in the arbitrary waveform generator. As shown in Fig. 1(b), there are two dominant noise components at approximately $(2\pi)82$ kHz ($\alpha = 0.1635$) and $(2\pi)164$ kHz ($\alpha = 0.3450$) that are too strong to be described by Eq. (2). According to Eq. (2), we see an exponential decay from 1 to 0.5 with a time-dependent rate $\gamma(t) = (1/t)\int_0^{\infty} d\omega S(\omega)F(\omega,\Omega,t)$. Generally, this is valid only if the PSD of noise varies gently as a function of ω. However, Fig. 1(b) suggests that, when $\Omega \approx (2\pi)82$ or $(2\pi)164$ kHz, P_s can be at least down to 0.3, smaller than the limit value 0.5 of Eq. (2). This means that we have to examine these two components of noise using another method.

III. DOMINANT NOISE CHARACTERIZATION

The strong coupled environment has already been discussed in some articles (e.g., Ref. [36]), where a discrete spectrum assumption is made. They express the PSD as a sum of discrete noises $S(\omega) = \sum_{k=1}^{N} S_k\delta(\omega - \omega_k)$ with S_k the noise strength at ω_k. This method is typically employed when studying some dominant components whose linewidth is relatively small, such as the noise at $(2\pi)50$ Hz and the harmonics coming from the power line [9]. In our system, the $(2\pi)82$ and $(2\pi)164$ kHz components of noise come from the modulation process of the etalon of the 729 nm Ti:sapphire laser. Because the electrical signal that drives the etalon has an absolutely narrower linewidth than several hertz, it is reasonable to assume the noise PSD as a δ function. However, instead of the PDD technique utilized in Refs. [9,36] to obtain S_k, we propose a method here to characterize the dominant noise components as well as the weaker coupling region around them where the state evolution is modulated by these components. We measure the evolution of P_s as a function of time t with Ω being set to around $(2\pi)82$ kHz, as shown in Fig. 2(a). We observe Rabi oscillations between $\pm X$ states that are similar to the case where a TLS is driven by (an)a (off-)resonant laser beam. Therefore, it is reasonable to make an analogy between driving lasers and these noise components, which are called laserlike noises (LLNs) in the rest of this paper. Generally, LLNs can be expressed as $f_D(t) = E_0\cos(\omega_0 t + \phi_0)$ in the time domain with central frequency $\omega_0 \approx (2\pi)82$ or $(2\pi)164$ kHz and amplitude E_0 whose exact values need to be extracted from the experimental data.

We write the Hamiltonian describing a TLS driven by LLNs in the interaction picture with respect to the frequency of the 729 nm laser as

$$H^{\mathrm{LLN}} = \tfrac{1}{2}\Omega\sigma_x + \tfrac{1}{2}\delta\Omega(t)\sigma_x + \tfrac{1}{2}f'(t)\sigma_z + \Omega_{\mathrm{LLN}}\cos(\omega_0 t + \phi_0)\sigma_z. \quad (3)$$

Here, $\Omega_{\mathrm{LLN}} = E_0/2$ represents the resonant Rabi frequency, $f'(t)$ is the remaining frequency noise that excludes the LLN components from $f(t)$, and $\delta\Omega(t)$ represents the power fluctuations of our 729 nm laser beam. The latter kind of noise is not introduced into the model in Sec. II because the exponential decay along the σ_x axis is immune to it. Here ϕ_0 shows the initial phase of LLNs for

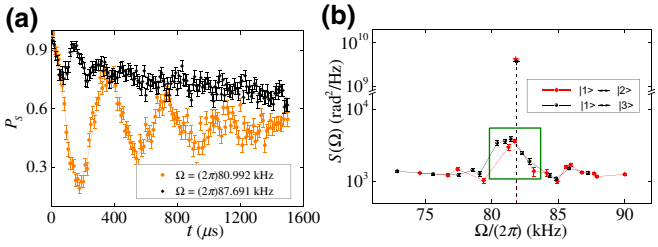

FIG. 2. Decoherence and the PSD of dominant noise components. (a) LLN-induced Rabi oscillations with different Ω around $(2\pi)82$ kHz. The solid curves are fittings using $\widetilde{\Gamma}_1$ and $\widetilde{\Gamma}_2$. Each point represents 200 experiments. (b) Fitting results of $\Omega_{\mathrm{LLN}}, \omega_0$ as well as $S(\Omega)$ of the $(2\pi)82$ kHz noise component. Each black circle and red diamond represents a fitting result at different Ω. The black triangle and red star represent the mean values of $\omega_0, \Omega_{\mathrm{LLN}}$ for each transition.

each run and is set as $\phi_0 = 0$ without introducing errors. We rewrite the static part of H^{LLN} in the rotating frame with $H_0 = \frac{1}{2}\omega_0 t\sigma_x$ as

$$H_{\mathrm{st}}^{\mathrm{LLN}} = -\tfrac{1}{2}\Delta\sigma_x + \tfrac{1}{2}\Omega_{\mathrm{LLN}}\sigma_z, \tag{4}$$

where $\Delta = \omega_0 - \Omega$ is the detuning. The evolution of a TLS under Eq. (4) is a rotation at the effective Rabi procession frequency $\Omega_R = \sqrt{\Omega_{\mathrm{LLN}}^2 + \Delta^2}$. Because of the noise $\frac{1}{2}f'(t)\sigma_z$ and $\frac{1}{2}\delta\Omega(t)\sigma_x$, it also experiences a longitudinal decoherence with the relaxation rate $\Gamma_1 = T_1^{-1} = (t/4\pi)\int_0^\infty d\omega S(\omega)\mathrm{sinc}^2[(\omega-\Omega)t/2] \approx S(\Omega)/2$ and pure dephasing with rates $\Gamma_\phi = S_{\delta\Omega}(0)/2$ and $\Gamma_v = S_{\delta\Omega}(\Omega_R)/2$ [37]. Here $S_{\delta\Omega}(\omega)$ is the PSD of $\delta\Omega(t)$. When $\Delta \neq 0$, the qubit dynamics is conveniently described in the alternate eigenbasis $\{\pm\widetilde{X}\}$ rotated from the conventional basis $\{\pm X\}$ by an angle $\eta = \arctan(\Omega_{\mathrm{LLN}}/\Delta)$. Here, we define two relaxation rates $\widetilde{\Gamma}_1$ and $\widetilde{\Gamma}_2$ that are analogous to Γ_1 and Γ_2 (the transverse relaxation rate). They correspond to the decay of longitudinal and transverse parts of the density matrix in the alternate basis, respectively. As a result, we obtain [38]

$$\widetilde{\Gamma}_1 = \frac{1+\cos^2\eta}{2}\Gamma_1 + \Gamma_v \sin^2\eta, \tag{5}$$

$$\widetilde{\Gamma}_2 = \frac{\widetilde{\Gamma}_1}{2} + \widetilde{\Gamma_\phi} = \frac{3-\cos^2\eta}{4}\Gamma_1 + \Gamma_\phi\cos^2\eta + \frac{1}{2}\Gamma_v\sin^2\eta, \tag{6}$$

where $\widetilde{\Gamma_\phi} = \frac{1}{2}\Gamma_1\sin^2\eta + \Gamma_\phi\cos^2\eta$. To simplify the model, we assume that $\Gamma_v = 0$ because the power of the 729 nm laser beam is stabilized in our system. Then we use Eqs. (5) and (6) to obtain the information $S(\Omega)$, Ω_{LLN}, and ω_0 by fitting with the LLN-driving Rabi oscillations, as shown in Fig. 2(a). Data are obtained by measuring P_s as a function of t. For each Ω, the LLN results in a Rabi oscillation with angular precession frequency Ω_R. To determine these parameters as precise as possible, we average the outputs of more than twenty Rabi oscillations for each noise component, and finally obtain $\Omega_{\mathrm{LLN1}} = (2\pi)2.842 \pm (2\pi)0.045$ kHz, $\omega_{01} = (2\pi)81.832 \pm (2\pi)0.055$ kHz for noise around $(2\pi)82$ kHz and $\Omega_{\mathrm{LLN2}} = (2\pi)3.362 \pm (2\pi)0.081$ kHz, $\omega_{02} = (2\pi)163.780 \pm (2\pi)0.057$ kHz for noise around $(2\pi)164$ kHz. Therefore, the PSD can be obtained: $S(\omega_{01}) = \pi\Omega_{\mathrm{LLN1}}^2 = (4.007 \pm 0.001) \times 10^9$ rad^2/Hz and $S(\omega_{02}) = (5.279 \pm 0.002) \times 10^9$ rad^2/Hz. Concerning these results, because the noise at ω_{02} is a harmonic of the other component, we observe that $2\omega_{01} \approx \omega_{02}$. As for $S(\omega_{01}) < S(\omega_{02})$, the reason is that the ω_{01} component is suppressed in our experimental setup. In Fig. 2(b), an example of how we get $S(\omega_{01})$ is given. The black triangle and red star show the averaged fitting results belonging to each transition. It is reasonable and convenient to determine the final value just by averaging them. Besides, the fitting results of $S(\Omega)$ near ω_{01} are also shown in Fig. 2(b). The red diamonds and black dots show the noise PSD for transitions $|1\rangle \leftrightarrow |2\rangle$ and $|1\rangle \leftrightarrow |3\rangle$, respectively. Because of the fitting errors, we find that some red diamonds show larger PSD than black circles for the same Ω. In order to

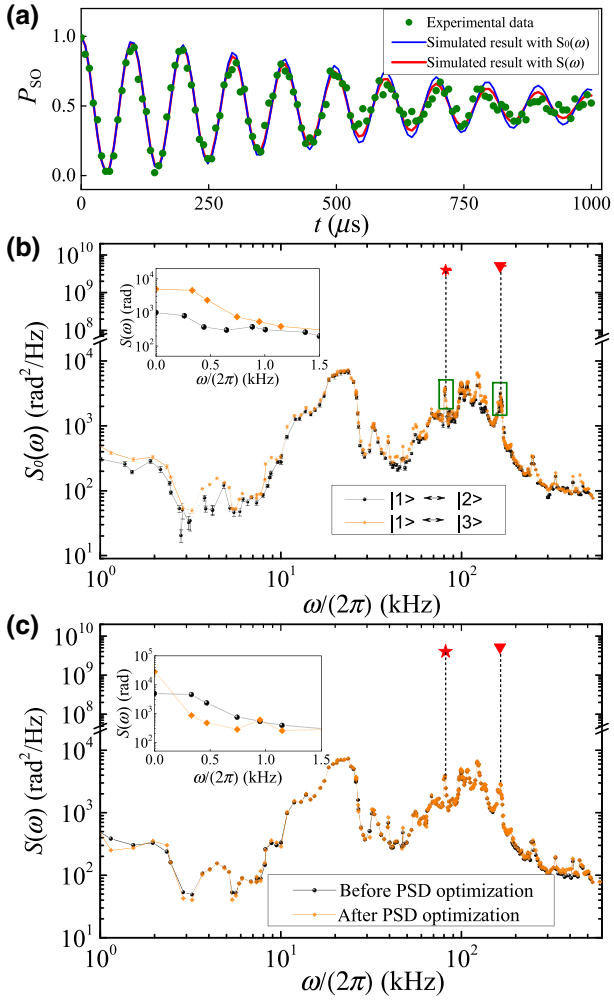

FIG. 3. Noise power spectral density. (a) Survival probability P_{so} of state $+X$ as a function of t. The oscillation results from the ac Stark shift difference explained in the main text. The blue and red curves are numerical simulations using $S_0(\omega)$ and $S(\omega)$ given in (b) and (c), respectively. Each point represents 200 experiments, and the error bars are not shown. (b) Experimentally determined noise PSD $S_0(\omega)$ over a range 0–$(2\pi)530$ kHz. The green rectangles enclose the same regions as in Fig. 2(b). The inset gives a detailed description for the part below $(2\pi)1.5$ kHz. (c) An example of $S(\omega)$ extrapolated from $S_0(\omega)$ with the gradient descent protocol for transition $|1\rangle \leftrightarrow |3\rangle$. The inset serves to show remarkable differences between $S_0(\omega)$ and $S(\omega)$ for the frequencies below $(2\pi)1.5$ kHz.

get the PSD of both noises, we assume that the PSD of magnetic noise in this region is a constant determined by the values outside the boundary (see Sec. IV and Fig. 4). The green rectangle in Fig. 2(b) encloses an area where an increasement appears when Ω tends towards ω_{01}. This may result from the power-noise contribution at frequency Ω_R (i.e., Γ_v) that is ignored above for simplicity. This means that these data only give the upper limit of $S(\Omega)$. On the other hand, it seems that Γ_v has negligible influence on the regions below 80 kHz and above 84 kHz because we observe well-matched joint points derived from different fitting approaches in Fig. 3(b). This in turn verifies the validity of our model.

IV. FULL-SPECTRUM ESTIMATION AND NOISE DISCRIMINATION

On the other hand, we study the rest of the noise spectrum by using the standard continuous dynamical decoupling technique where the evolution of P_s is described by Eq. (2). Different from the experiments measuring two dominant noise components above where the 729 nm laser power remains the same in $Y_{\pi/2}$ and driving evolution processes [see the inset in Fig. 1(b)], here we use laser pulses with different powers in these stages, so that we can save measurement time while the PSD $S(\omega)$ of the noise is captured. It can be described in more detail. We carefully locate the laser power at a value where the noise PSD is relatively small based on Fig. 1(b), such as $\Omega_S = (2\pi)200$ kHz whose $\pi/2$ pulse lasts 1.25 μs. Then these kinds of $\pi/2$ pulses are employed as $Y_{\pi/2}$ in all experiments where different Ω are used in the driving evolution processes. In this way, we do not need to calculate and check the $\pi/2$-pulse time when Ω is changed. However, it should be mentioned that, due to this difference in laser power between $Y_{\pi/2}$ and the driving evolution stages, and thus a different ac Stark shift, a Ramsey-like oscillation will be introduced when we monitor the survival probability on state $+X$ as a function of t:

$$P_{\rm so} = \frac{1}{2} + \frac{1}{2}\cos(\delta_A t)\exp\left[-\int_0^\infty d\omega S(\omega)F(\omega,\Omega,t)\right]. \tag{7}$$

Here δ_A is the ac Stark shift difference.

In Fig. 3(a) we show an example of this oscillation decay. The experimental data are represented by green circles. We then use the filtering property of the sequence to characterize the noise spectrum. We note that the filter is sufficiently narrow about Ω so that we can treat the noise as a constant $S(\Omega)$ within its bandwidth $1/t$ and approximate Eq. (7) as $P_{\rm so} = \frac{1}{2} + \frac{1}{2}\cos(\delta_A t)\exp[-S(\Omega)/2t]$. Utilizing this rectangular approximation approach, the data can be fitted to get $S(\Omega)$. As a result, we obtain the noise PSD $S_0(\omega)$ over a frequency range 0–$(2\pi)530$ kHz by combining the other two dominant noise components, as shown in Fig. 3(b). We observe a peak approximately at $(2\pi)23.5$ kHz belonging to the frequency noise of the laser, and a sharp increase below $(2\pi)1$ kHz (the inset) coming from the magnetic field fluctuations. We also observe a stronger noise for transition $|1\rangle \leftrightarrow |3\rangle$ (orange diamonds) than for transition $|1\rangle \leftrightarrow |2\rangle$ (black circles), which is consistent with our assumption.

To extend the accuracy of the measured noise PSD, we propose a gradient descent protocol based on matching to the experimental oscillation decay curves. Define an objective function as the sum of the squared error between the experimentally measured decay $P_s(t_j)$ and the calculated decay rule $P'_s(t_j) = \frac{1}{2} + \frac{1}{2}\cos(\delta_A t)\exp[-\int_0^\infty d\omega S'(\omega)F(\omega,\Omega,t_j)]$ for a given $S'(\omega)$:

$$J = \sum_{j=1}^{M}[P_s(t_j) - P'_s(t_j)]^2. \tag{8}$$

We then calculate the gradient of this function $\partial J/\partial S'(\omega_i)$ for any target frequency ω_i. The gradient is used to update the initial $S'(\omega)$ towards a closer matching of all the experimental and calculated decays. Finally, a comparison between the optimized PSD $S(\omega)$ (orange diamonds) and $S_0(\omega)$ (black circles) corresponding to $|1\rangle \leftrightarrow |3\rangle$ is shown in Fig. 3(c). We easily find that the gradient optimization has the most remarkable effects for the extreme points of $S(\omega)$, especially those between sharp increases and decreases. The reason is simple. In these intervals, the rectangular approximation approach may not be valid anymore because $S(\omega)$ cannot be replaced by $S(\Omega)$ within the filter bandwidth. After obtaining the optimized $S(\omega)$, we also verify its correctness. In Fig. 3(a), we give the simulated evolution $P_{\rm so}$ based on $S_0(\omega)$ (blue curve) and $S(\omega)$ (red curve). It is obvious that the red curve matches the data points better, which shows a greater fidelity of $S(\omega)$.

To get the PSD of the laser frequency noise, we utilize the $S(\omega)$ for both transitions $|1\rangle \leftrightarrow |2\rangle$ and $|1\rangle \leftrightarrow |3\rangle$ obtained above whose difference can be used to speculate the magnetic field fluctuations. According to atomic physics, the magnetic field noise induced energy level shift changes the transition circular frequency by $f_B(t) = [\mu_B \delta B(t)/\hbar][g_j(D_{5/2})m' - g_j(S_{1/2})m]$, where μ_B is the Bohr magneton, the g_j are the Lande g factors, and m', m are the magnetic quantum numbers of the $D_{5/2}$ and $S_{1/2}$ states, respectively. Here $\delta B(t)$ represents the magnetic field strength fluctuations. For $^{40}Ca^+$, $g_j(S_{1/2}) \approx 2$ and $g_j(D_{5/2}) \approx 1.2$, so that the PSD of $\delta B(t)$ can be expressed as $S_{\delta B}(\omega) = [S_{1\leftrightarrow 3}(\omega) - S_{1\leftrightarrow 2}(\omega)]\hbar^2/(24 \times 0.16\mu_B^2)$. Next we obtain the PSD of the laser frequency noise by $S_L(\omega) = S_{1\leftrightarrow 2}(\omega) - [S_{1\leftrightarrow 3}(\omega) - S_{1\leftrightarrow 2}(\omega)]/24$, as shown in Fig. 4. To get from the discrete data points in Fig. 3(c) to the continuous lines here, we employ the interpolation method. In Fig. 4, we observe a complex PSD for

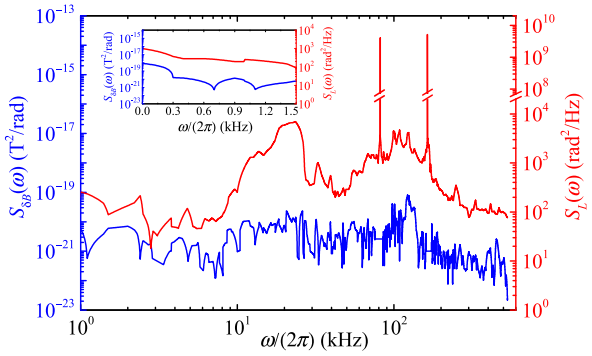

FIG. 4. Noise discrimination. The PSD of laser and magnetic field noises are represented by the red and blue lines, respectively. The inset shows the details of the PSD below $(2\pi)1.5$ kHz.

both kinds of noise that cannot be described by a single line type, such as $1/\omega^{\alpha}$ used in many articles. We also see a small interconnected trend between $S_{\delta B}(\omega)$ and $S_L(\omega)$ in some peaks, such as $\omega \approx (2\pi)23.5$ kHz. In our opinion, this is primarily derived from the limited accuracy at these points where the fitting error is considerable.

V. COMPARED TO THE BEAT-NOTE SCHEME

Alternatively, in order to characterize the frequency noise of this Ti:sapphire laser, we beat it with a distinct diode laser at 729 nm. The electrical spectra of the beat-note signals are presented in Fig. 5(a) as red curves. In fact, they are power spectral densities of the output electrical signal i of the photodiode that is used to convert the combined bichromatic light field [the amplitude of the target (reference) laser is E_1 (E_2)] to the photocurrent. The carrier frequency of the beat note has been shifted to 0 Hz from 5.36 MHz, which represents the frequency difference between the two lasers. Note that, due to the dominant noise components from the photodiode, there are several asymmetrical spikes with respect to 0 Hz. For clarity, we mark the spikes with green stars in the figure.

In fact, we can find the relation between the beat-note signal $S_i(\omega)$ and the frequency noise PSD of lasers by the equation [39]

$$S_i(\omega) = \left(\frac{\alpha E_1 E_2}{2}\right)^2 \int_{-\infty}^{\infty} d\tau \cos(\omega - \omega_0)\tau \times \exp\left\{-\frac{\tau^2}{4\pi}\int_{-\infty}^{\infty} d\omega'[S_1(\omega') + S_2(\omega')] \times \mathrm{sinc}^2\left(\frac{\omega'\tau}{2}\right)\right\}, \quad (9)$$

where ω_0 is the frequency difference between the two lasers, α shows the photoelectric conversion coefficient of the photodiode, $S_1(\omega)$ and $S_2(\omega)$ represent the noise power

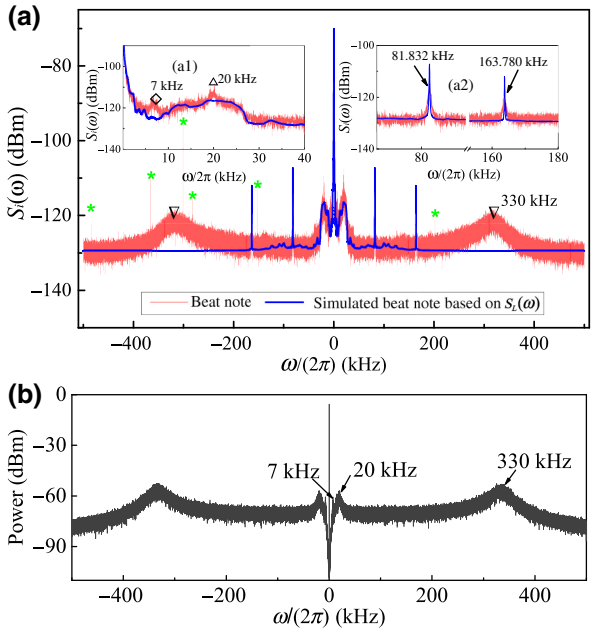

FIG. 5. (a) Electrical spectra of the (simulated) laser beat-note signals. Red curves show the beat note between our Ti:sapphire laser under test and a diode laser at 729 nm, while the blue curves represent the simulated beat-note result according to Eq. (9) by setting $S_1(\omega) = S_L(\omega)$ and $S_2(\omega) = 0$. Note that there are several peaks marked with green stars. They are from the photodiode instead of two laser beams. Usually, the beat note is determined by the noise from both lasers. This is exactly the reason why two curves have a divergent behavior at ± 7 kHz [diamond in inset (a1)], ± 20 kHz [triangle in inset (a1)], and ± 330 kHz (upside-down triangles) where the frequency noise from the diode laser dominates. The insets give more details for the regions (a1) 0.1 kHz $\sim$ 40 kHz and (a2) 70 kHz $\sim$ 180 kHz. We see good matching between the two kinds of curves, such as the dominant noise components centered at 81.832 and 163.5 kHz in inset (a2). (b) The PDH error spectrum of the 729 nm diode laser is measured with a rf spectral analyzer.

spectral densities of the laser under test and the reference laser, respectively. Equation (9) implies that the beat-note result in Fig. 5(a) is determined by the noise of both lasers. Furthermore, from this beat note, we cannot tell the contributions of each laser apart if we do not have any prior information, as mentioned in Sec. I. To make a comparison, let us consider the case where the target laser is beat with an ideal laser, i.e., $S_1(\omega) = S_L(\omega)$ and $S_2(\omega) = 0$; then we can obtain a simulated beat-note result [see the blue curves in Fig. 5(a)]. This simulated beat note actually only contains the frequency noise information of the target Ti:sapphire laser. By comparing it with the experimental beat note in Fig. 5(a), we observe that the two curves match very well except for three distinct components centered at ± 7 kHz [marked as a diamond in inset (a1)], ± 20 kHz [the triangle in inset (a1)], and ± 330 kHz (upside-down triangles in the main plot). Because these

components have been proved to be from the diode laser according to the Pound-Drever-Hall (PDH) error signal spectrum [Fig. 5(b)] measured by a rf spectrum analyzer (for more information about the PDH error signal spectrum, see Ref. [40]), we conclude that the validity of our model and result expressed in Secs. III–IV are confirmed. In order to show more details in low-frequency regions, we also provide two insets showing good matching between two curves in the ranges (a1) 0.1 kHz $\sim$ 40 kHz and (a2) 70 kHz $\sim$ 180 kHz. In inset (a2) we find that the central frequencies of dominant noise components at 81.832 and 163.780 kHz are accurately estimated in Sec. III, while the strength seems to be less convincing because the peaks of the beat note are wider and lower. In fact, this property follows from the convolution with other noise components such as that at 330 kHz from the diode laser. Therefore, the validity of our result should not be denied just by this difference. To be more precise, this actually exposes a shortcoming of the beat-note method.

VI. CONCLUSION

We employ the continuous dynamical decoupling protocol in this work to estimate the laser frequency noise spectrum. It is based on controlling the system-environment interaction by applying a continuous driving field along the σ_x axis to the system after initializing the system on the $+X$ state. This driving field and the corresponding Rabi frequency Ω create the dressed states $+X$ and $-X$ between which the transition frequency is Ω in the interaction picture. Because the noise $f(t)$ works along the σ_z axis, it actually causes a state transition between the $+X$ and $-X$ states. In this way, the system will suffer less from the most noisy parts of the frequency bands except for those around Ω as long as the noise spectrum $S(\Omega)$ is non-negligible. By using this filtering property of controlling sequences and the gradient descent algorithm, we directly characterize the overall noise PSD up to $(2\pi)530$ kHz, which in turn enables the design of coherent control that targets a specific noise component. However, in our case of laser noise, there are two dominant components centered at $(2\pi)81.832$ and $(2\pi)163.780$ kHz that are too strong to use this filter function method. Instead, we propose an approach that regards these noises as driving lasers performed in the space spanned by the dressed states $\pm X$ after being initialized on $+X$. To simplify the model, a discreteness assumption is made. The LLNs-induced decay Rabi oscillation in the $\{+X, -X\}$ space can give information about the central frequency and strength of this noise. On the other hand, due to the equivalent timescales of both the laser noise and magnetic field noise acting on the system, we finally obtain the PSD of each by encoding the qubit on different Zeeman sublevels of $^2D_{5/2}$. Especially, this method is of great significance for characterizing the laser noise from the mixed noise. Furthermore, by comparing with the beat-note signal, our result is verified. This indicates that we do not need to employ the optical heterodyne approach anymore for which at least hundreds of kilometers of optical fibers or several similar lasers are required.

ACKNOWLEDGMENTS

This work is supported by the National Basic Research Program of China under Grant No. 2016YFA0301903 and the National Natural Science Foundation of China under Grants No. 61632021, No. 11904402, and No. 12004430.

M.Z. and Y.X. contributed equally to this work.

[1] F. Arute, K. Arya, R. Babbush, D. Bacon, J. C. Bardin, R. Barends, R. Biswas, S. Boixo, F. G. S. L. Brandao, D. A. Buell, *et al.*, Quantum supremacy using a programmable superconducting processor, Nature **574**, 505 (2019).

[2] N. Ofek, A. Petrenko, R. Heeres, P. Reinhold, Z. Leghtas, B. Vlastakis, Y. Liu, L. Frunzio, S. M. Girvin, L. Jiang, *et al.*, Extending the lifetime of a quantum bit with error correction in superconducting circuits, Nature **536**, 441 (2016).

[3] B. Merkel, K. Thirumalai, J. E. Tarlton, V. M. Schäfer, C. J. Ballance, T. P. Harty, and D. M. Lucas, Magnetic field stabilization system for atomic physics experiments, Rev. Sci. Instrum. **90**, 044702 (2019).

[4] T. Gullion, D. B. Baker, and M. S. Conradi, New, compensated carr-purcell sequences, J. Magn. Reson. **89**, 479 (1990).0022-2364

[5] C. A. Ryan, J. S. Hodges, and D. G. Cory, Robust Decoupling Techniques to Extend Quantum Coherence in Diamond, Phys. Rev. Lett. **105**, 200402 (2010).

[6] A. Ajoy, G. A. Alvarez, and D. Suter, Optimal pulse spacing for dynamical decoupling in the presence of a purely dephasing spin bath, Phys. Rev. A **83**, 032303 (2011).

[7] A. M. Souza, G. A. Alvarez, and D. Suter, Robust Dynamical Decoupling for Quantum Computing and Quantum Memory, Phys. Rev. Lett. **106**, 240501 (2011).

[8] B. Pokharel, N. Anand, B. Fortman, and D. A. Lidar, Demonstration of Fidelity Improvement Using Dynamical Decoupling with Superconducting Qubits, Phys. Rev. Lett. **121**, 220502 (2018).

[9] Y. Wang, M. Um, J. Zhang, S. An, M. Lyu, J. N. Zhang, L. M. Duan, D. Yum, and K. Kim, Single-qubit quantum memory exceeding ten-minute coherence time, Nat. Photonics **11**, 646 (2017).

[10] A. Bermudez, P. O. Schmidt, M. B. Plenio, and A. Retzker, Robust trapped-ion quantum logic gates by continuous dynamical decoupling, Phys. Rev. A **85**, 040302(R) (2012).

[11] J. M. Cai, B. Naydenov, R. Pfeiffer, L. P. Mcguinness, K. D. Jahnke, F. Jelezko, M. B. Plenio, and A. Retzker, Robust dynamical decoupling with concatenated continuous driving, New J. Phys. **14**, 113023 (2012).

[12] D. Farfurnik, N. Aharon, I. Cohen, Y. Hovav, A. Retzker, and N. Bar-Gill, Experimental realization of time-dependent phase-modulated continuous dynamical decoupling, Phys. Rev. A **96**, 013850 (2017).

[13] X. Xu, Z. Wang, C. Duan, P. Huang, P. Wang, Y. Wang, N. Xu, X. Kong, F. Shi, X. Rong, and J. Du, Coherence-Protected Quantum Gate by Continuous Dynamical Decoupling in Diamond, Phys. Rev. Lett. **109**, 070502 (2012).

[14] N. Timoney, I. Baumgart, M. Johanning, A. F. Varon, M. B. Plenio, A. Retzker, and C. Wunderlich, Quantum gates and memory using microwave-dressed states, Nature **476**, 185 (2011).

[15] D. A. Golter, T. K. Baldwin, and H. Wang, Protecting a Solid-State Spin from Decoherence Using Dressed Spin States, Phys. Rev. Lett. **113**, 237601 (2014).

[16] A. Stark, N. Aharon, T. Unden, D. Louzon, A. Huck, A. Retzker, U. L. Andersen, and F. Jelezko, Narrow-bandwidth sensing of high-frequency fields with continuous dynamical decoupling, Nat. Commun. **8**, 1105 (2017).

[17] B. G. Christensen, C. D. Wilen, A. Opremcak, J. Nelson, F. Schlenker, C. H. Zimonick, L. Faoro, L. B. Ioffe, Y. J. Rosen, J. L. DuBois, B. L. T. Plourde, and R. McDermott, Anomalous charge noise in superconducting qubits, Phys. Rev. B **100**, 140503(R) (2019).

[18] K. W. Chan, W. Huang, C. H. Yang, J. C. C. Hwang, B. Hensen, T. Tanttu, F. E. Hudson, K. M. Itoh, A. Laucht, A. Morello, *et al.*, Assessment of a Silicon Quantum Dot Spin Qubit Environment via Noise Spectroscopy, Phys. Rev. Appl. **10**, 044017 (2018).

[19] T. N. Huynh, L. Nguyen, and L. P. Barry, phase noise characterization of SGDBR lasers using Phase modulation detection method with delayed self-heterodyne measurements, J. Lightwave Technol. **31**, 1300 (2013).

[20] A. Walsh, J. Odowd, V. Bessler, K. Shi, F. Smyth, J. M. Dailey, B. Kelleher, L. P. Barry, and A. D. Ellis, Characterization of time-resolved laser differential phase using 3D complementary cumulative distribution functions, Opt. Lett. **37**, 1769 (2012).

[21] X. Xie, R. Bouchand, D. Nicolodi, M. Lours, C. Alexandre, and Y. L. Coq, Phase noise characterization of sub-hertz linewidth lasers via digital cross correlation, Opt. Lett. **42**, 1217 (2017).

[22] T. Yuge, S. Sasaki, and Y. Hirayama, Measurement of the Noise Spectrum Using a Multiple-Pulse Sequence, Phys. Rev. Lett. **107**, 170504 (2011).

[23] J. Bylander, S. Gustavsson, F. Yan, F. Yoshihara, K. Harrabi, G. Fitch, D. G. Cory, Y. Nakamura, J. S. Tsai, and W. D. Oliver, Noise spectroscopy through dynamical decoupling with a superconducting flux qubit, Nat. Phys. **7**, 565 (2011).

[24] L. M. Norris, D. Lucarelli, V. M. Frey, S. Mavadia, M. J. Biercuk, and L. Viola, Optimally band-limited spectroscopy of control noise using a qubit sensor, Phys. Rev. A **98**, 032315 (2018).

[25] P. Cappellaro, J. S. Hodges, T. F. Havel, and D. G. Cory, Principles of control for decoherence-free subsystems, Journal of Chemical Physics **125**, 044514 (2006).

[26] Y. Sung, F. Beaudoin, L. M. Norris, F. Yan, D. Kim, J. Y. Qiu, U. Von Lupke, J. Yoder, T. P. Orlando, S. Gustavsson, *et al.*, Non-gaussian noise spectroscopy with a superconducting qubit sensor, Nat. Commun. **10**, 1 (2019).

[27] I. Almog, Y. Sagi, G. Gordon, G. Bensky, G. Kurizki, and N. Davidson, Direct measurement of the system-environment coupling as a tool for understanding decoherence and dynamical decoupling, Journal of Physics B **44**, 154006 (2011).

[28] M. Mukhtar, W. T. Soh, T. B. Saw, and J. Gong, Protecting unknown two-qubit entangled states by nesting Uhrig's dynamical decoupling sequences, Phys. Rev. A **82**, 052338 (2010).

[29] J. Zhang, W. Wu, C. Wu, J. Miao, Y. Xie, B. Ou, and P. Chen, Discrimination and estimation for dephasing sources of trapped ion qubits, Applied Physics B **126**, 20 (2020).

[30] G. A. Alvarez and D. Suter, Measuring the Spectrum of Colored Noise by Dynamical Decoupling, Phys. Rev. Lett. **107**, 230501 (2011).

[31] M. Bishof, X. Zhang, M. J. Martin, and J. Ye, Optical Spectrum Analyzer with Quantum Limited Noise Floor, Phys. Rev. Lett. **111**, 093604 (2013).

[32] Z. H. Wang, W. Zhang, A. M. Tyryshkin, S. A. Lyon, J. W. Ager, E. E. Haller, and V. V. Dobrovitski, Effect of pulse error accumulation on dynamical decoupling of the electron spins of phosphorus donors in silicon, Phys. Rev. B **85**, 085206 (2012).

[33] L.-Z. He, M.-C. Zhang, C.-W. Wu, Y. Xie, W. Wu, and P.-X. Chen, Effects of imperfect pulses on dynamical decoupling using quantum trajectory method, Chinese Physics B **27**, 120303 (2018).

[34] F. Yan, S. Gustavsson, J. Bylander, X. Jin, F. Yoshihara, D. G. Cory, Y. Nakamura, T. P. Orlando, and W. D. Oliver, Rotating-frame relaxation as a noise spectrum analyser of a superconducting qubit undergoing driven evolution, Nat. Commun. **4**, 2337 (2013).

[35] K. Willick, D. K. Park, and J. Baugh, Efficient continuous-wave noise spectroscopy beyond weak coupling, Phys. Rev. A **98**, 013414 (2018).

[36] S. Kotler, N. Akerman, Y. Glickman, and R. Ozeri, Nonlinear Single-Spin Spectrum Analyzer, Phys. Rev. Lett. **110**, 110503 (2013).

[37] E. Geva, R. Kosloff, and J. L. Skinner, On the relaxation of a two-level system driven by a strong electromagnetic field, Journal of Chemical Physics **102**, 8541 (1995).

[38] G. Ithier, E. Collin, P. Joyez, P. J. Meeson, D. Vion, D. Esteve, F. Chiarello, A. Shnirman, Y. Makhlin, J. Schriefl, *et al.*, Decoherence in a superconducting quantum bit circuit, Phys. Rev. B **72**, 134519 (2005).

[39] G. M. Stephan, T. T. Tam, S. Blin, P. Besnard, and M. Tetu, Laser line shape and spectral density of frequency noise, Phys. Rev. A **71**, 043809 (2005).

[40] The error signal in the PDH frequency stabilization process represents the nonlinear response to the laser frequency fluctuations and can be analyzed by a rf spectral analyzer. However, this noise analysis method is usually not employed as a direct and precise measurement approach of the noise PSD for two reasons. First, its spectrum is different from the frequency noise PSD, and only gives general information about the noise components, such as the position and modulated relative strength. Second, due to the limitations of the rf spectral analyzer, this method cannot provide a precise measurement of noise in the low-frequency region. For example, the operating range of our rf spectral analyzer (KEYSIGHT: CXA Signal Analyzer N9000B) is 9 kHz to 3 GHz, so the noise components below 9 kHz cannot be measured with gratifying accuracy.